OPTICS

Engineered entropic forces allow ultrastrong dynamical backaction

Andreas Sawadsky, Raymond A. Harrison, Glen I. Harris, Walter W. Wasserman, Yasmine L. Sfendla, Warwick P. Bowen*, Christopher G. Baker

When confined within an optical cavity light can exert strong radiation pressure forces. Combined with dynamical backaction, this enables important processes, such as laser cooling, and applications ranging from precision sensors to quantum memories and interfaces. However, the magnitude of radiation pressure forces is constrained by the energy mismatch between photons and phonons. Here, we overcome this barrier using entropic forces arising from the absorption of light. We show that entropic forces can exceed the radiation pressure force by eight orders of magnitude and demonstrate this using a superfluid helium third-sound resonator. We develop a framework to engineer the dynamical backaction from entropic forces, applying it to achieve phonon lasing with a threshold three orders of magnitude lower than previous work. Our results present a pathway to exploit entropic forces in quantum devices and to study nonlinear fluid phenomena such as turbulence and solitons.

INTRODUCTION

Light generally interacts only weakly with mechanical objects. However, it has been shown that strong interactions can be achieved by confining the light in an optical cavity and using a low-dissipation mechanical resonance (*1*). These cavity optomechanical devices have enabled applications such as laser amplification and cooling of mechanical motion (*2*) and technologies such as precision sensors (*3*–*6*). It has even been possible to reach quantum regimes, where the interaction can create nonclassical states of light and of mechanical motion (*7*, *8*) and can enable quantum memories and interfaces, among other quantum technologies (*9*, *10*).

Usually, the optical forces are achieved using radiation pressure or electrostriction (*1*, *2*). In these cases, it is generally considered desirable to operate in the resolved sideband regime, for which the cavity lifetime is longer than the period of the mechanical resonance (*10*, *11*). However, this prevents multiple scattering processes so that each incident photon can only add or subtract a maximum of one phonon (*11*). This introduces a fundamental barrier to the strength of forces that can be imparted by light—the maximum efficiency with which energy may be converted from light into mechanical motion is given by the ratio of mechanical to optical frequencies. This ratio is typically in the range of 10^{-9} to 10^{-5}. Multiple scattering is possible in the reverse, nonresolved sideband regime (*10*, *11*). However, in this regime, the interaction is suppressed due to the mismatch between the time scales of cavity decay and mechanical motion (*12*).

Optical forces can alternatively be applied via entropy gradients, instead of energy gradients. Entropic forces are common in nature, for example, explaining many molecular forces (*13*, *14*) and the restoring force of a stretched rubber band (*15*). Entropic optical forces arise due to absorption of photons and the resulting heat transfer. Generally known as photothermal forces, they can allow dynamical backaction effects such as laser cooling of mechanical motion (*16*), including into the quantum regime (*17*, *18*). They can evade the compromise between the number and time scale of interactions that is present for radiation pressure. Operating in the nonresolved sideband regime allows multiphonon scattering, while the time scale of the interaction can be controlled via the delay introduced during heat transfer (*16*, *19*–*21*). This promises orders of magnitude stronger optical forces but has yet to be achieved. This is, in part, due to the complexities of calculating the strength of the interaction and designing devices to leverage it (*21*).

Here, we demonstrate entropic forces in an optomechanical device that are eight orders of magnitude stronger than would be possible with radiation pressure alone. We use them to demonstrate optomechanical phonon lasing with a threshold power of only a few picowatts, a factor of 2000 lower than has been shown before (*22*). This phonon laser can be viewed as a microscale thermodynamic heat engine. We show that its efficiency—while low due to the small temperature differential introduced by photon absorption—is nonetheless around a hundred times higher than previous nanomechanical heat engines (*23*, *24*) and could be increased above 10% in purpose-designed devices. Crucial to enabling these results, we develop a broadly applicable methodology to model optomechanical entropic forces and the dynamical backaction they cause.

Our optomechanical device exploits third sound resonances of a superfluid helium thin film as the mechanical element (*25*–*28*). This choice of mechanical element allows the precise engineering of entropic forces, leveraging both entropy-driven fountain pressure, which exists only in superfluids, and the ability to tune the thermal properties of the system over many orders of magnitude via small changes in temperature, film thickness, and geometry.

It is natural to ask whether the strong forcing achieved here is due to a unique property of the superfluid fountain pressure force. We note however that the fountain pressure per absorbed photon is of similar magnitude to the thermoelastic stress which would occur in a crystalline material (see the Supplementary Materials). It is thus primarily the engineered ability to collect the thermal energy and operate with near optimally time-delayed

---

ARC Centre of Excellence for Engineered Quantum Systems, School of Mathematics and Physics, University of Queensland, St. Lucia, QLD 4072, Australia.
*Corresponding author. Email: w.bowen@uq.edu.au

forcing, combined with the much higher compliance of liquids compared to solids (*29*–*31*) which is responsible for the ultralow threshold observed here and not a fundamentally stronger nature of the fountain pressure force in superfluid helium. This makes these results broadly applicable to photothermally and electrothermally driven systems and different fluids.

RESULTS

Modeling and optimizing entropic forces

Photon absorption events cause a local change in the superfluid temperature, which introduces a fountain (entropic) pressure between hot and cold regions. This drives superfluid flow toward the heat source (*32*–*34*) [the thermomechanical effect (*35*)] and, in bulk superfluid helium, drives normal fluid counterflow. These flows exert forces on the superfluid that can be used to drive superfluid sound modes (*27*). Similar to other thermomechanical forces (*16*), the forces are not instantaneous. Rather, they react over the thermal response time τ, which depends on both the properties of the superfluid and the vessel in which it resides. The time delay introduces dynamical backaction that can be used to both cool and amplify the motion of the superfluid (*27*, *29*). Optimization of this entropic backaction requires both that the fountain pressure is maximized and that the condition $\Omega\tau \sim 1$ is met, where Ω is the resonance frequency of the superfluid mode. This condition corresponds to the optimal delay in the optical force for efficient energy transfer (*17*, *20*). The fountain pressure is given by $\Delta p = \rho S \Delta T$, where ρ, ΔT, and S are, respectively, the superfluid density, local temperature change, and entropy (*33*). Using this relation and extending known results for other thermomechanical forces (*17*–*19*), we find that the effective dynamical backaction force is given by $F = \rho S \Delta T \mathscr{A} \times \left(\frac{\Omega\tau}{1+\Omega^2\tau^2}\right)$, where $\mathscr{A}$ is the effective area of the sound mode, including any spatial mismatch between the mode and the fountain pressure force.

To model the entropic forces and entropic backaction, we consider the general system geometry shown in Fig. 1A. This consists of a superfluid reservoir in contact with a solid substrate and a vapor-phase environment. These, in turn, are in contact with a thermal bath at temperature T. Light interacts with the system via photon absorption events which, due to the vanishingly small optical absorption of superfluid helium (*36*), are assumed to occur only within the substrate. Heat from absorption events can dissipate either directly into the thermal bath or by propagating into the superfluid through the interfacial Kapitza resistance and then via evaporation of helium into the vapor-phase.

The Kapitza conductance (R_K^{-1}) scales with the cube of temperature, while the effective thermal conductance of evaporation (R_{vap}^{-1}) increases exponentially with temperature (see the Supplementary Materials). Small temperature changes can also change the superfluid entropy and thermal conductivity of the substrate by orders of magnitude, while the geometry of the superfluid-coated device can greatly affect the temperature change ΔT induced by optical absorption, the frequency of the sound mode, and the thermal anchoring of the superfluid. As we will see in the following, these strong dependencies provide a powerful means to either leverage strong fountain pressure forces at low temperatures or suppress them at high temperatures so that the unitary radiation pressure interaction can be exploited.

To enable quantitative predictions, we develop an electric circuit analog model (Fig. 1A, right). This model combines a thermal circuit (red) that represents heat flow, a fluid-flow circuit (blue) that represents superfluid mass flow, and a lumped-element resistor-inductor-capacitor (RLC) circuit that represents the superfluid sound mode. The thermal and fluid-flow circuits are connected via an effective capacitor which accounts for the fact that a temperature difference drives a superflow via the fountain pressure, while conversely a superflow affects the temperature via the mechanocaloric effect (*37*). The current, voltage, resistance, and capacitance in the electric circuit are, respectively, the analogs of heat flow $\dot{Q}$, temperature T, thermal resistance, and heat capacity, while a chemical potential difference μ drives a mass flow $\dot{m}$ in the superfluid. For a given geometry and temperature, we determine the parameters of the circuit using a combination of existing data and finite-element modeling. We are then able to simulate the dynamics of the sound mode, including entropic forcing and entropic backaction. The simulation ultimately yields a complex transfer function, providing both the amplitude and phase response of the superfluid sound mode (see section S2).

As a specific application of our analog electric circuit model, we consider a few nanometer-thick superfluid film self-assembled on a microsphere (Fig. 1B). Because of the thinness of the film, only the superfluid component can move, as the normal fluid component is viscously clamped (*34*). The superfluid component sustains third sound waves, similar to shallow water waves, due to the van der Waals restoring force between the superfluid and the microsphere surface (*27*, *28*, *38*–*40*). The microsphere is suspended on a stem that is attached to a flat substrate. The substrate creates an effective boundary, confining resonant third sound modes. These "stem modes" present as oscillations in the film thickness that flow back and forth along the stem, as illustrated in Fig. 1B (i and ii). Their resonance frequencies Ω can be conveniently tuned by changing the length l of the stem or by tuning the film thickness and therefore the strength of the van der Waals force. Their motion can be optically driven and observed by exploiting optical whispering gallery mode (WGM) resonances that exist within the microsphere (*27*).

We choose to study the fundamental stem mode, which features a single antinode at the microsphere and a single node at the substrate. Since the antinode coincides with the position of the optical WGM, its motion is well coupled to the WGM resonance. Modeling shows that in our regime, the thermal conductivity is such that optical absorption events act to raise the temperature of the entire microsphere-stem system, so that the effective area $\mathscr{A}$ over which the force is applied is, to good approximation, equal to the total surface area of the system. Using these assumptions, we calculate all parameters of the analog circuit model in section S2. This allows us to predict the effective entropic dynamical backaction force F.

Our model predicts that there exists an optimal combination of temperature and mechanical resonance frequency to maximize the dynamical backaction force. We find that the optimal resonance frequency coincides with the resonance frequency of the fundamental stem mode if a stem length of $l \sim 2$ mm is chosen and that, for this stem length, the optimal temperature of $T \simeq 250$ mK is easily experimentally accessible. To remove any dependence on laser power, we normalize the dynamical backaction force F by the radiation pressure force $F_{\text{rad}} = n_{\text{cav}}\hbar G$ (*11*), where n_{cav} is the number of photons within the resonator and $G/2\pi = 0.2$ GHz/nm the radiation pressure

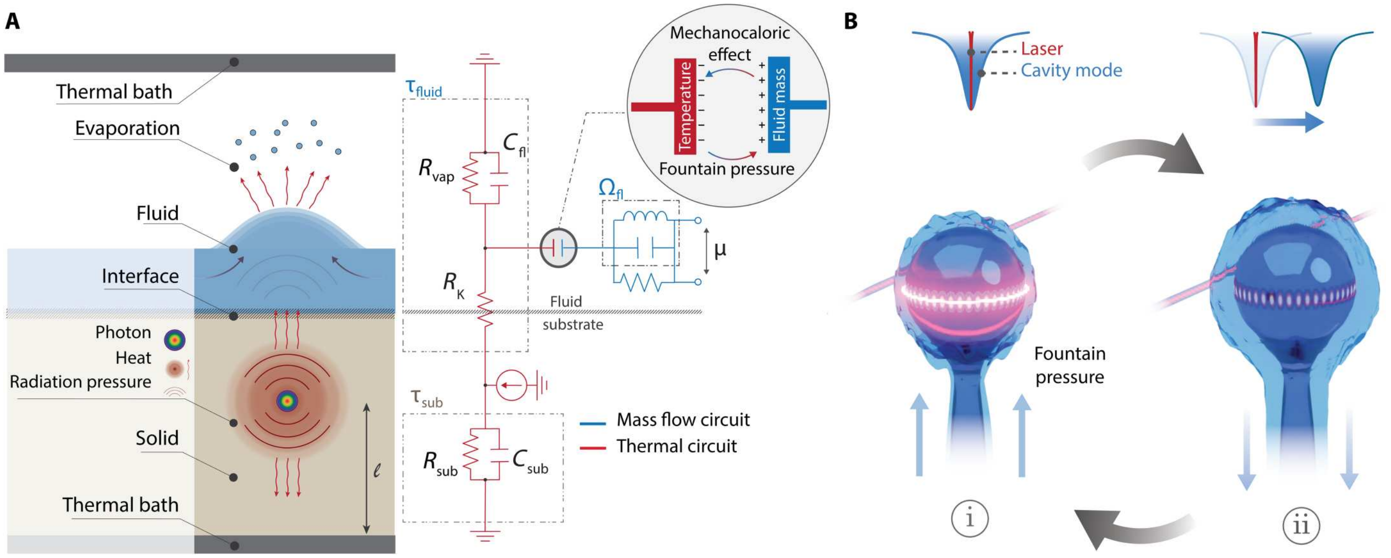

Fig. 1. Modeling of entropic forces. (**A**) Left: Cross-sectional schematic showing the superfluid and heat flow in response to photon absorption. Right: Thermal equivalent circuit (red) coupled to the superfluid mass flow circuit (blue). R, thermal resistance; C, heat capacity; μ, chemical potential; K, Kapitza; sub, substrate; vap, vapor; fl, fluid (see the Supplementary Materials). (**B**) Superfluid optomechanical resonator used in the experiments: fiber-coupled silica microsphere on a silica stem, covered by a ~24-nm superfluid film (blue). Illustration of the optomechanical feedback loop between superfluid motion and intracavity power responsible for dynamical backaction (*11*).

optomechanical coupling rate (see section S1). This provides the dimensionless figure of merit $f_M = F/F_{\text{rad}}$ shown in Fig. 2A as a function of both temperature and mechanical resonance frequency, for a microsphere WGM resonator that we fabricated which has a stem length of $l = 1.8$ mm. As can be seen, f_M is predicted to be sharply peaked, varying by more than seven orders of magnitude as the temperature is changed by a factor of 10 and also varying strongly with resonance frequency. At its optimum, the fountain pressure force is predicted to be over eight orders of magnitude larger than the radiation pressure force.

To further illustrate the substantial gains that can be achieved through optimization, we calculate the same figure of merit for the microdisk superfluid optomechanical system reported in (*29*). In that work, where the fountain pressure was simply introduced as an ad hoc fitting parameter to account for the discrepancy between the experimentally observed behavior and the theory

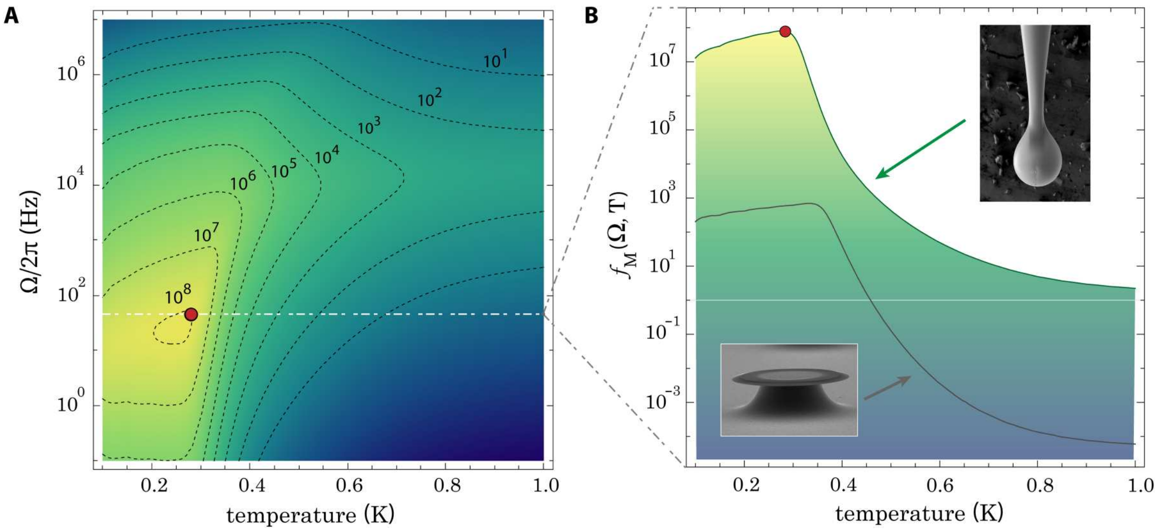

Fig. 2. Optimized entropic forcing. (**A**) Contour plot of the figure of merit $f_M(\Omega, T)$, indicating the optimal operating point for enhanced photothermal backaction, as a function of cryostat temperature T and third sound frequency $\Omega/2\pi$. (**B**) Cut through the white dashed line in (A), showing the figure of merit $f_M(2\pi \times 72, T)$ for our microsphere resonator (solid line). The gray line plots the same figure of merit for our previous silica microdisk experimental geometry (*29*) (calculated with $\Omega = 2\pi \times 7$ MHz), for which the optomechanical forces should be entirely dominated by radiation pressure at temperatures above 500 mK. The horizontal line marks the boundary between the fountain pressure and the radiation pressure-dominated regimes (situated above and below, respectively). Red dot in (A) and (B) marks our experimental operating point.

accounting for radiation pressure alone, phonon lasing occurred on a high-order Brillouin sound mode at $\Omega/2\pi = 7$ MHz. This is shown in Fig. 2B as a function of temperature, alongside the microsphere for comparison. While the trends are similar, the peak value is close to five orders of magnitude lower for the microdisk. Our modeling moreover shows that for temperatures in excess of 500 mK, the superfluid becomes much more strongly thermally anchored to the cryostat through its vapor phase than to the substrate. This effectively thermally decouples the superfluid from the microresonator, switching off the fountain pressure interaction. Temperature control therefore provides a useful lever (unexploited in previous work) to either leverage strong fountain pressure forces at low temperatures or focus on the unitary radiation pressure interaction at higher temperatures.

Experimental validation

To validate the predictions of our model, we locate our microsphere WGM device within a superfluid-tight enclosure whose temperature can be precisely tuned between $T = 10$ mK and $T = 1.5$ K. A narrow capillary enables the film thickness to be changed in situ, ranging from a few atomic monolayers to a maximum reached at the saturated vapor pressure, where the sphere is uniformly coated with a $d \simeq 24$-nm-thick superfluid film (~80 atomic layers), see the Supplementary Materials. By controlling the bath temperature T and the stem-mode frequency (through superfluid film thickness), we are able to operate at the near-optimal experimental setting where the fountain pressure is maximized and the mechanical frequency matches the thermal response, with $\Omega\tau = 0.94$, marked by the red dot in Fig. 2 (A and B).

We optically excite the WGM resonator via evanescent coupling of 1554-nm light from a tapered optical fiber placed in its close proximity, achieving critical coupling to a WGM with intrinsic dissipation rate $\kappa_i/2\pi = 15$ MHz. The time-delayed fountain pressure forcing modifies the dynamics of the fundamental stem mode through the introduction of an effective optomechanical damping rate Γ_{ent}. The sign of this modification may be positive, leading to cooling of the sound mode (*27*), or negative, leading to amplification (*29*). In the latter case, phonon lasing occurs once the magnitude of optomechanical (anti-) damping exceeds the intrinsic acoustic damping rate Γ (*10*, *16*, *17*, *20*). A measure of the strength of the light-superfluid interaction is provided by the power and intracavity photon number at which this regime is reached.

We use the heterodyne readout scheme shown in Fig. 3A to measure the power spectra of superfluid oscillation for various input powers. These are shown in Fig. 4A. The sharp peak observed at the expected frequency of the fundamental stem mode is characteristic of phonon lasing for cryostat temperatures over the range of 100 to 500 mK. We find that the phonon lasing peak appears for the lowest laser powers at a temperature of around 280 mK, consistent with the predictions of our model. At this temperature, the peak is visible even for powers as low as a few picowatts, while for the higher power of 78 pW, more than 10 higher harmonics are seen (see Fig. 4B). These harmonics indicate that the phonon lasing has reached motional amplitudes that are sufficiently large to detune the optical cavity away from resonance with the excitation field, thereby introducing a transduction nonlinearity.

To confirm that the observed behavior is phonon lasing and to constrain the threshold optical drive power, we sweep the laser wavelength over the cavity resonance (from blue- to red-detuned) for various input powers. A characteristic feature of dynamical backaction is that the sign of the optomechanical damping it introduces is opposite on either side of the resonance. We therefore expect to observe lasing on one side of resonance and cooling on the other. For each power and detuning, we measure the power spectrum to determine the peak of the dynamic response of the stem mode. In Fig. 4C, we plot the normalized peak power spectral density versus detuning for input powers of 680 fW, 3.4 pW, 6.8 pW, and 68 pW. At the lowest input power of 680 fW, the measured mode amplitude (blue dots) is low and symmetric around the cavity resonance. This indicates limited dynamical back action. At an input power of 3.4 pW, the measured mode amplitude is about four times higher on the heating side (blue-detuned) compare to the cooling side (red-detuned), indicating that phonon lasing is occurring. At this point, the superfluid oscillator is in a regime of large coherent oscillations with an amplitude of ~1 Å, modulating the intensity of the transmitted optical field by more than 60%. This provides further confirmation that phonon lasing is occurring, since, in the absence of other nonlinearities, a large modulation is required to suppress the exponential growth in phonon lasing to a constant amplitude in the steady state. The modulation does this by reducing the average intracavity power and therefore the steady-state gain of the phonon lasing process (*41*). At higher powers again, both the asymmetry and lasing amplitude increase further. These results are in good agreement with numerical simulations (black line), solving the coupled equations of motion for the intracavity field, superfluid motional amplitude, and temperature (see section S3 for more details). Our results indicate that the phonon lasing threshold is in the range of 1 to 3.4 pW, corresponding to an average of less than 0.2 intracavity photons. This threshold is more than three orders of magnitude lower than previously reported values for optically driven optomechanical resonators (*22*).

Prior experiments have used radiation pressure, electrostrictive, electrothermal, and photothermal forces. Most of them form a cluster with microwatt-range threshold powers and picogram-range masses (see section S5). Only electrothermally driven carbon nanotube resonators reach thresholds approaching a picowatt (*23*, *24*). An important attribute that enables this is their attogram-level mass. This exceptionally low mass allows large motional amplitudes to be driven with small forces. By exploiting engineered entropic backaction, our results operate in a vastly different parameter space, breaking the trend between threshold power and mass. Our nanogram resonator mass is eight orders of magnitude larger than electrothermally driven systems.

Thermodynamic efficiency

The larger mass of our system compared to other extremely low threshold phonon lasers is partly offset by the superfluid resonator's lower frequency, since the stored mechanical energy scales as $m_{\text{eff}}\Omega^2$. A more complete picture emerges when comparing the systems' thermodynamic efficiencies, which account for the overall optical to acoustical energy conversion.

Our optomechanical phonon laser can be thought of as a heat engine converting heat into mechanical work, with the superfluid film acting as the working medium, the cryostat acting as the cold reservoir, and the heated region of the microsphere acting as the hot reservoir. We can estimate its thermodynamic efficiency η by comparing the mechanical power P_{mech} supplied to the superfluid oscillator to sustain its oscillations to the optical power dissipated in the

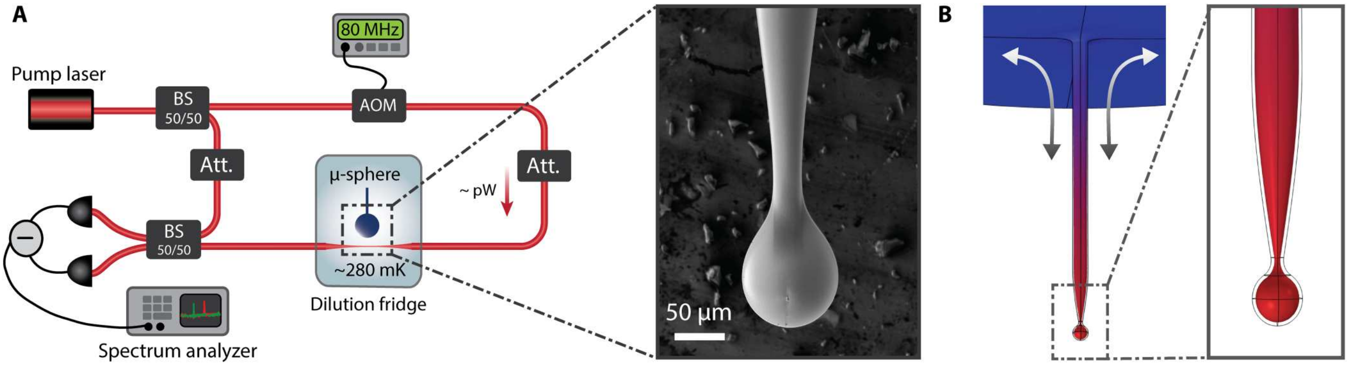

Fig. 3. Experimental setup. (**A**) Simplified heterodyne experimental setup schematic, including beam splitters (BS), attenuator (att.), and acousto-optic modulator (AOM). Inset shows a scanning electron microscopy image of the microsphere. (**B**) Finite element simulation showing the fundamental superfluid third sound mode confined to the surface of the microsphere resonator (including stem), obtained by solving the Helmholtz equation on the resonator's outer surface (see section S1). Inset shows the displacement profile at the level of the spherical tip, where the WGM field is located.

resonator P_{abs}. At an input power of $P = 6.8$ pW, well above the onset of lasing, this yields $\eta = \frac{P_{\text{mech}}}{P_{\text{abs}}} = \frac{1}{2} m_{\text{eff}} \Omega^2 x^2 \Gamma / (P \times \alpha_{\text{abs}}) \simeq 10^{-5}$ (see section S5).

This can be compared to the Carnot limit $\eta_{\max} = 1 - \frac{T_C}{T_H}$ determined by the temperature of the hot and cold reservoirs T_H and T_C. Here, $T_C = T$ is the cryostat temperature, and $T_H = T + \Delta T$ is the temperature of the heated microresonator. At $P = 6.8$ pW, our numerical simulations show that $T_C = 284.0$ mK and $T_H = 284.4$ mK (see section S3 and fig. S9), such that $\eta_{\max} \simeq 10^{-3}$. This means that the system operates within two orders of magnitude of the thermodynamic limit. One reason that it does not reach this limit is that the hot and cold reservoirs are thermally linked through the stem, leading to substantial thermal losses.

While the efficiency we achieve is low, to our knowledge, it is nonetheless the highest optical-to-mechanical conversion efficiency reported in an optomechanical device operating at optical frequencies. The nonlinear radiation pressure scattering interaction between a photon of frequency ω and a mechanical oscillator of frequency Ω leads to an energy transfer $\hbar\Omega$ in the resolved sideband regime [where $\Omega > \kappa$ (*10*, *11*)], providing an upper bound of $\eta \le \Omega/\omega$. Gigahertz frequency optomechanical crystals (*22*) operate in a regime where this fraction reaches up to $\Omega/\omega \sim 2.5 \times 10^{-5}$; however, the total efficiency is suppressed by a factor of $Gx/\omega \ll 1$ due to the low rate at which photons enter the cavity via the upper motional sideband (*11*). Alternatively, when operating at very large motional amplitudes (*42*) or in the unresolved sideband regime ($\kappa \gg \Omega$), each photon can generate many phonons—corresponding to the generation of a large number of higher-order motional sidebands. This has been used to excite mechanical oscillators to very large amplitudes, corresponding to occupations upward of 10^{12} phonons (*12*), but the efficiency was limited by the lower phonon energy. In all of the above cases, as well as for low threshold microtoroid resonators (*1*), efficiencies are in the 10^{-8} to 10^{-7} range. A similar overall efficiency $\eta \sim 10^{-5}$ has only been reported in the radio frequency regime through multi photon-phonon scattering between GHz microwave photons and a megahertz oscillator, i.e., in a case where the mismatch between optical and mechanical frequencies was only of order 1000 and not 10^{12} like in the current work (*43*).

Our efficiency is additionally substantially larger than that of photothermally driven resonators reported in the literature (*16*, *20*), where η was on the order of 10^{-12}. It is also two orders of magnitude higher than the efficiency of 10^{-7} achieved for an electrothermally driven carbon nanotube in (*24*), which has the lowest previously reported phonon lasing threshold (see section S5).

The higher efficiency reported here can be understood by considering that our optomechanical device operates in the unresolved sideband regime, enabling efficient on-resonance pumping of the cavity while simultaneously operating in the resolved sideband regime as far as the time delay is concerned. In radiation pressure–driven systems, the optimal time-delayed forcing criterion $\Omega\tau_{\text{rp}} \sim 1$ is equivalent to $\Omega \sim \kappa$ (resolved sideband regime), which consequently requires inefficient off-resonant driving of the cavity. Here, since the delay is no longer provided by the finite lifetime of the photons in the cavity $\tau_{\text{rp}} = 1/\kappa$ but by an independently controllable thermal response time τ, this tension is relieved, enabling a combination of on resonance driving and efficient dynamical backaction $\Omega\tau \sim 1$. This allows us to use a broad optical resonance enabling a greater dynamic range (*41*) and larger mechanical amplitudes to be reached while maintaining a large time delay τ for the optical forcing (equivalent to what would be achieved by an optical cavity with Q of 2×10^{12}).

The thermodynamic efficiency could be further improved by reducing the volume of the resonator. The microsphere volume, including the stem, is on the order of $10^6\ \mu\text{m}^3$. This can be reduced by approximately six orders of magnitude to $\sim 1\ \mu\text{m}^2$ through the use of smaller mode volume resonators such as photonic crystal resonators (*44*) or high index WGM cavities (*45*). The reduced thermal mass then leads to a smaller ratio of T_C/T_H and predicted efficiencies $\eta_{\max} > 10$ %, commensurate with the highest reported values for the efficiency of superfluid fountain effect pumps (*46*).

DISCUSSION

As discussed earlier, at the operating point of our experiments, the entropic forces are around 10^8 stronger than the radiation pressure forces. Moreover, the dimensionless term $\left(\frac{\Omega\tau_{\text{rp}}}{1+\Omega^2\tau_{\text{rp}}^2}\right)$, where $\tau_{\text{rp}} = 1/\kappa$ is the photon decay rate, which quantifies the efficiency of the time-delayed radiation-pressure forcing for dynamical backaction (*10*, *16*–*19*), is only 2×10^{-6} for the acoustic mode considered here. In

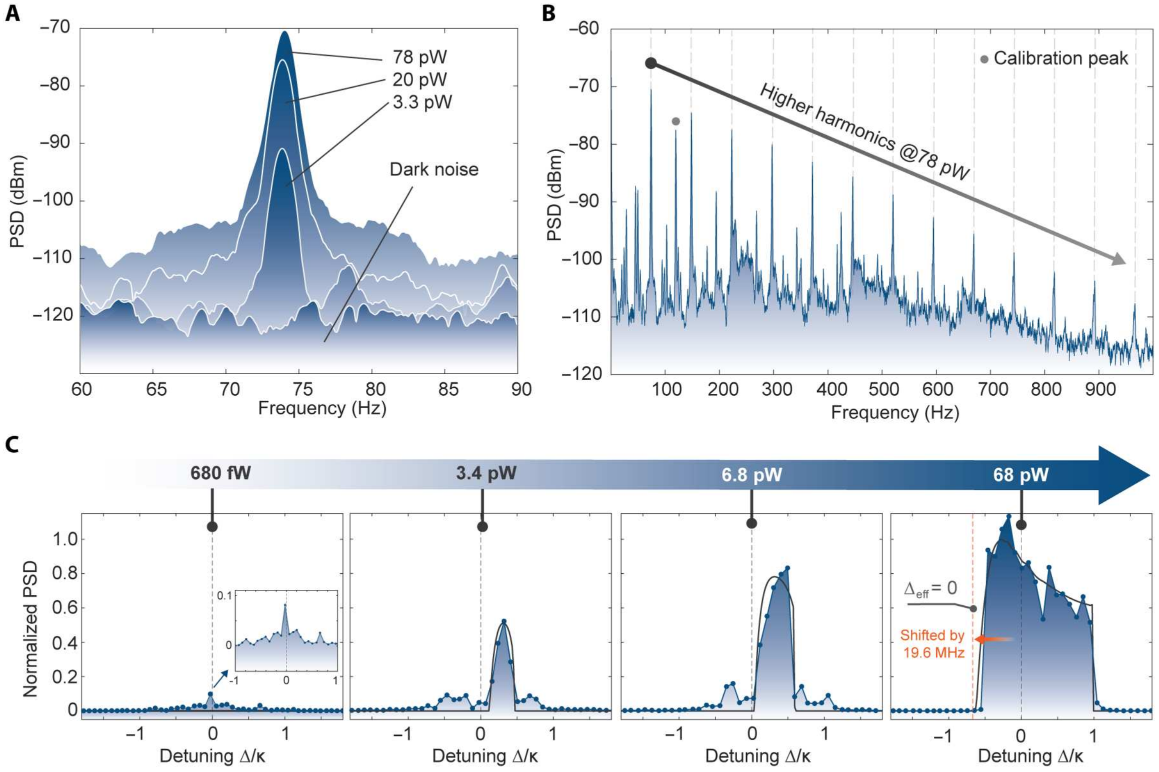

Fig. 4. Entropic backaction-driven phonon lasing. (**A**) Power spectral density (PSD) of the fundamental stem mode at $\Omega_M/2\pi = 72$ Hz lasing at different input powers. (**B**) Broader power spectrum at an input power of 78 pW showing 12 higher harmonics of the fundamental mode Ω_M. The peak marked by the gray dot is an introduced calibration peak. (**C**) Lasing threshold measurement and the corresponding ODE simulations. Each subfigure corresponds to different input power, which is increasing from 680 fW to 68 pW. Each blue point corresponds to the peak power spectral density of the superfluid mode for a laser detuning Δ with respect to the cavity resonance, while the black line shows the results of the ODE simulation. We attribute the larger magnitude of the peak near zero detuning in the leftmost panel to experimental noise. At 68 pW, the lasing appears to occur for both positive and negative cavity detunings. This is due to steady-state optical heating of the WGM resonator by around 3.6 mK above $T = 284$ mK (see fig. S10). This DC heating causes an influx of superfluid shifting the resonance frequency by 19.6 MHz, in good agreement with simulations, and corresponds to a tunability of 288 GHz/μW.

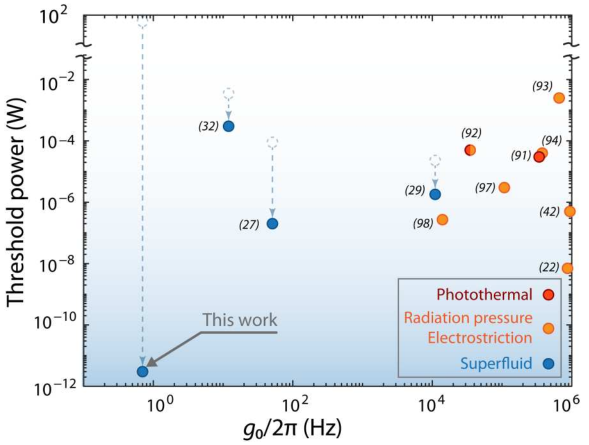

Fig. 5. Comparison to the state of the art. Phonon lasing thresholds of different optomechanical experiments plotted versus radiation pressure single photon optomechanical coupling rate g_0. For the superfluid data points, the hollow circles indicate the predicted lasing threshold in the presence of radiation pressure forcing alone, underscoring the gains achieved through entropic forcing. Details on the reference publication for each point can be found in section S5.

contrast, the equivalent term for fountain pressure is of order 1/2. Combined, this means that the optimized fountain pressure dynamical backaction is over 13 orders of magnitude more effective. This is illustrated in Fig. 5, where prior experiments are compared as a function of their single-photon optomechanical coupling rate g_0, a normalization-independent figure of merit (*11*). Entropic forces thus enable the efficient driving of low-frequency superfluid acoustic modes in a regime where the radiation pressure fails. We expect this to have important consequences for the study of superfluid nonlinear hydrodynamical phenomena such as solitonic behavior (*47*) and vortex stirring (*28*), where the ability to drive and monitor large amplitude wave motion without boiling the film is critical. Our work provides the combination of high-precision optomechanical readout—capable of measuring superfluid waves with submonolayer thickness precision and micrometer spatial resolution—with an actuation capability sufficiently strong to reach the highly nonlinear regime where the wave amplitude becomes comparable to the film thickness (see the Supplementary Materials).

While superfluid helium is characterized by its viscosity-free flow, we emphasize that the results obtained here do not rely on exceptionally low fluidic dissipation and are applicable to conventional fluids. The low-threshold phonon lasing is achieved despite a very modest acoustic quality factor $Q = 55$, dominated by acoustic radiation losses (see the Supplementary Materials). This Q value is of comparable magnitude to that measured for instance in kilohertz-frequency capillary resonances of micrometer-sized octane microdroplets used to demonstrate the first ripplon laser (*48*). Photothermal effects in conventional fluids have also garnered attention for applications ranging from chiral optofluidics with plasmonic metasurfaces (*49*) to pump-free micromixing (*50*) and cell sorting (*51*) through photothermal vortices.

Compared to solids, fluids provide a pathway toward strongly enhanced light-matter interactions, thanks to their compliant interfaces. Early work by Ashkin and Dziedzic (*52*) used radiation pressure from a focussed laser beam to deform an air-liquid interface, using the direction of the deflection (outward) to answer open questions about the momentum of photons in a dielectric. The malleability of liquid-liquid and liquid-air interfaces has also been leveraged in optofluidic devices such as adaptive lenses and "lab-on-chip" applications (*53*), as well as for fluidic optomechanical resonators (*54*–*56*), the generation of giant optical nonlinearities (*57*), and transformable optical cavities (*30*)—which have been proposed to reach the single-photon nonlinear regime (*31*). With the thick (d = 24 nm) film considered here, the van der Waals pressure $P_{\mathrm{vdW}} = \frac{\rho\alpha_{\mathrm{vdw}}}{d^3}$, which opposes surface deformation and plays the role of the Young's modulus in a solid, is two billion times softer than the underlying silica sphere (*40*). The consequence of this compliance extends here beyond dynamical backaction into large static deformations and optical tunability. Steady-state optical heating of the WGM resonator causes a DC fountain pressure that locally thickens the film. This changes the effective radius of the cavity, shifting the resonance frequency. At an input power of 68 pW, a DC heating of around 3.6 mK above the bath temperature of T = 284 mK (see fig. S10) shifts the resonance by 19.6 MHz, as shown in Fig. 4C. This shift corresponds to an exceptionally high all-optical tunability of 288 GHz/μW, nearly three orders of magnitude larger than that achieved with purpose-built all optical wavelength routing systems based on mechanically compliant nano-optomechanical resonators (*58*). It is also well in excess of the highest reported values for thermal tuning of microresonators (0.26 GHz/μW) (*59*)—albeit with the constraints of cryogenic operation and reduced response rate and dynamic range—underscoring the strength of this optomechanical interaction. In the scenario where the volume of the resonator is reduced to the order of ∼1 μm^2, its thermal mass becomes dominated by the helium film itself, and the achievable fountain pressure per absorbed photon takes the simple, temperature independent expression $P_{\mathrm{fp}} \simeq \frac{\hbar\,\omega}{3\,V_{\mathrm{He}}}$. Using this relation, we find that optical frequency shifts larger than κ are achievable for a single absorbed photon, potentially providing an alternate approach to single photon detection (see section S8).

Last, this work may lay the groundwork for transformable phononics, where optically defined acoustic circuits may be formed on demand. DC radiation pressure and/or fountain pressure contributions can substantially thicken the film, as mentioned in the context of optical tuning. This thickening also reduces the speed of sound $c_3 = \sqrt{3\alpha_{\mathrm{vdW}} d^{-3}}$ within the optically defined "bulge." Thus, much like an optical waveguide where light is trapped in a higher refractive (lower speed) medium, this could be used to optically trap sound waves (*60*). Optomechanical backaction in this regime would represent an original form of dynamical backaction between the intensity of light within a cavity and the shape of the mechanical eigenmodes that it creates rather than with the momentum of an independently defined mechanical resonator.

MATERIALS AND METHODS

Experimental setup

The microsphere resonator is formed by melting the tapered end of a silica single-mode fiber (SMF-28) in a fusion splicer. It is then mounted by its non-reflown end inside a superfluid-tight sample chamber within a dilution refrigerator at a temperature T = 284 mK. Infrared laser light (λ = 1554 nm) from a low-noise erbium-doped fiber laser is evanescently coupled into the microsphere via a tapered optical fiber (*27*). Helium gas is injected via a capillary to form a d = 24-nm-thick saturated superfluid ^{4}He film covering the microsphere resonator (see section S1 for more details) (*27*, *29*, *32*). The optical WGMs have an evanescent component which extends outside the resonator and are therefore sensitive to the refractive index perturbation caused by the presence and motion of the superfluid (*40*). This leads to a frequency shift of the WGM resonances $\Delta\omega_0 = G \times d$, where $G/2\pi = 0.2 \pm 0.01$ GHz/nm is the optomechanical coupling rate (see the Supplementary Materials). High sensitivity optical readout of the superfluid's acoustic modes is performed with a heterodyne detection scheme with a local oscillator field offset by 80 MHz (*29*), as shown in Fig. 3A. Because of the nine orders of magnitude difference between probe and local oscillator beam powers (picowatt versus milliwatt), care must be taken to avoid any back reflections, even as small as those occurring on the facets of the balanced detector. This is done here with a circulator positioned after the microsphere (not shown in Fig. 3A).

Supplementary Materials

This PDF file includes:
Supplementary files and scripts
Figs. S1 to S16
Tables S1 to S4
References

REFERENCES AND NOTES

1. T. Kippenberg, H. Rokhsari, T. Carmon, A. Scherer, K. Vahala, Analysis of radiation-pressure induced mechanical oscillation of an optical microcavity. *Phys. Rev. Lett.* **95**, 033901 (2005).
2. J. Chan, T. P. M. Alegre, A. H. Safavi-Naeini, J. T. Hill, A. Krause, S. Gröblacher, M. Aspelmeyer, O. Painter, Laser cooling of a nanomechanical oscillator into its quantum ground state. *Nature* **478**, 89–92 (2011).
3. A. G. Krause, M. Winger, T. D. Blasius, Q. Lin, O. Painter, A high-resolution microchip optomechanical accelerometer. *Nat. Photonics* **6**, 768–772 (2012).
4. S. Basiri-Esfahani, A. Armin, S. Forstner, W. P. Bowen, Precision ultrasound sensing on a chip. *Nat. Commun.* **10**, 132 (2019).
5. T. Purdy, K. Grutter, K. Srinivasan, J. Taylor, Quantum correlations from a room-temperature optomechanical cavity. *Science* **356**, 1265–1268 (2017).
6. S. Forstner, E. Sheridan, J. Knittel, C. L. Humphreys, G. A. Brawley, H. Rubinsztein-Dunlop, W. P. Bowen, Ultrasensitive optomechanical magnetometry. *Adv. Mater.* **26**, 6348–6353 (2014).
7. A. H. Safavi-Naeini, S. Gröblacher, J. T. Hill, J. Chan, M. Aspelmeyer, O. Painter, Squeezed light from a silicon micromechanical resonator. *Nature* **500**, 185–189 (2013).
8. R. Riedinger, A. Wallucks, I. Marinković, C. Löschnauer, M. Aspelmeyer, S. Hong, S. Gröblacher, Remote quantum entanglement between two micromechanical oscillators. *Nature* **556**, 473–477 (2018).

9. R. Delaney, M. Urmey, S. Mittal, B. Brubaker, J. Kindem, P. Burns, C. Regal, K. Lehnert, Superconducting-qubit readout via low-backaction electro-optic transduction. *Nature* **606**, 489–493 (2022).
10. W. P. Bowen, G. J. Milburn, Quantum optomechanics, (CRC Press, Boca Raton, ed. 1, 2015).
11. M. Aspelmeyer, T. J. Kippenberg, F. Marquardt, Cavity optomechanics. *Rev. Mod. Phys.* **86**, 1391–1452 (2014).
12. M. Bagheri, M. Poot, M. Li, W. P. H. Pernice, H. X. Tang, Dynamic manipulation of nanomechanical resonators in the high-amplitude regime and non-volatile mechanical memory operation. *Nat. Nanotechnol.* **6**, 726–732 (2011).
13. S. Asakura, F. Oosawa, On interaction between two bodies immersed in a solution of macromolecules. *J. Chem. Phys.* **22**, 1255–1256 (1954).
14. X. Liu, M. M. Skanata, D. Stein, Entropic cages for trapping dna near a nanopore. *Nat. Commun.* **6**, 6222 (2015).
15. L. G. Treloar, *The physics of rubber elasticity*, (Oxford Univ. Press, 1975).
16. C. H. Metzger, K. Karrai, Cavity cooling of a microlever. *Nature* **432**, 1002–1005 (2004).
17. J. Restrepo, J. Gabelli, C. Ciuti, I. Favero, Classical and quantum theory of photothermal cavity cooling of a mechanical oscillator. *C. R. Phys.* **12**, 860–870 (2011).
18. S. De Liberato, N. Lambert, F. Nori, Quantum noise in photothermal cooling. *Phys. Rev. A* **83**, 033809 (2011).
19. C. Metzger, I. Favero, A. Ortlieb, K. Karrai, Optical self cooling of a deformable Fabry-Perot cavity in the classical limit. *Phys. Rev. B* **78**, 035309 (2008).
20. C. Metzger, M. Ludwig, C. Neuenhahn, A. Ortlieb, I. Favero, K. Karrai, F. Marquardt, Self-induced oscillations in an optomechanical system driven by bolometric backaction. *Phys. Rev. Lett.* **101**, 133903 (2008).
21. A. G. Primo, C. M. Kersul, R. Benevides, N. C. Carvalho, M. Ménard, N. C. Frateschi, P.-L. de Assis, G. S. Wiederhecker, T. P. Mayer Alegre, Accurate modeling and characterization of photothermal forces in optomechanics. *APL Photonics* **6**, 086101 (2021).
22. S. M. Meenehan, J. D. Cohen, S. Gröblacher, J. T. Hill, A. H. Safavi-Naeini, M. Aspelmeyer, O. Painter, Silicon optomechanical crystal resonator at millikelvin temperatures. *Phys. Rev. A* **90**, 011803 (2014).
23. Y. Wen, N. Ares, F. J. Schupp, T. Pei, G. A. D. Briggs, E. A. Laird, A coherent nanomechanical oscillator driven by single-electron tunnelling. *Nat. Phys.* **16**, 75–82 (2020).
24. C. Urgell, W. Yang, S. L. De Bonis, C. Samanta, M. J. Esplandiu, Q. Dong, Y. Jin, A. Bachtold, Cooling and self-oscillation in a nanotube electromechanical resonator. *Nat. Phys.* **16**, 32–37 (2020).
25. K. R. Atkins, Third and fourth sound in liquid Helium II. *Phys. Rev.* **113**, 962–965 (1959).
26. F. M. Ellis, L. Li, Quantum swirling of superfluid helium films. *Phys. Rev. Lett.* **71**, 1577–1580 (1993).
27. G. I. Harris, D. L. McAuslan, E. Sheridan, Y. Sachkou, C. Baker, W. P. Bowen, Laser cooling and control of excitations in superfluid helium. *Nat. Phys.* **12**, 788–793 (2016).
28. Y. P. Sachkou, C. G. Baker, G. I. Harris, O. R. Stockdale, S. Forstner, M. T. Reeves, X. He, D. L. McAuslan, A. S. Bradley, M. J. Davis, W. P. Bowen, Coherent vortex dynamics in a strongly interacting superfluid on a silicon chip. *Science* **366**, 1480–1485 (2019).
29. X. He, G. I. Harris, C. G. Baker, A. Sawadsky, Y. L. Sfendla, Y. P. Sachkou, S. Forstner, W. P. Bowen, Strong optical coupling through superfluid Brillouin lasing. *Nat. Phys.* **16**, 417–421 (2020).
30. M. Douvidzon, S. Maayani, H. Nagar, T. Admon, V. Shuvayev, L. Yang, L. Deych, Y. Roichman, T. Carmon, Toward transformable photonics: Reversible deforming soft cavities, controlling their resonance split and directional emission. *APL Photonics* **6**, 071304 (2021).
31. A. Lee, P. Zhang, Y. Xu, S. Jung, Radiation pressure-induced nonlinearity in a microdroplet. *Opt. Express* **28**, 12675–12687 (2020).
32. D. McAuslan, G. Harris, C. Baker, Y. Sachkou, X. He, E. Sheridan, W. Bowen, Microphotonic forces from superfluid flow. *Phys. Rev. X* **6**, 021012 (2016).
33. H. London, Thermodynamics of the thermomechanical effect of liquid He II. *Proc. R. Soc. London Series A Math. Phys. Sci.* **171**, 484–496 (1939).
34. C. Enss, S. Hunklinger, *Low-Temperature Physics,* (Springer Science & Business Media, 2005).
35. J. F. Allen, H. Jones, New phenomena connected with heat flow in helium II. *Nature* **141**, 243–244 (1938).
36. M. A. Weilert, D. L. Whitaker, H. J. Maris, G. M. Seidel, Laser levitation of superfluid helium. *J. Low Temp. Phys.* **98**, 17–35 (1995).
37. K. R. Atkins, B. Rosenbaum, H. Seki, Evaporation effects during superflow of liquid helium II. *Phys. Rev.* **113**, 751–754 (1959).
38. F. M. Ellis, H. Luo, Observation of the persistent-current splitting of a third-sound resonator. *Phys. Rev. B* **39**, 2703–2706 (1989).
39. A. M. R. Schechter, R. W. Simmonds, R. E. Packard, J. C. Davis, Observation of 'third sound' in superfluid 3He. *Nature* **396**, 554–557 (1998).
40. C. G. Baker, G. I. Harris, D. L. McAuslan, Y. Sachkou, X. He, W. P. Bowen, Theoretical framework for thin film superfluid optomechanics: Towards the quantum regime. *New J. Phys.* **18**, 123025 (2016).
41. M. Poot, K. Y. Fong, M. Bagheri, W. H. P. Pernice, H. X. Tang, Backaction limits on self-sustained optomechanical oscillations. *Phys. Rev. A* **86**, 053826 (2012).
42. A. G. Krause, J. T. Hill, M. Ludwig, A. H. Safavi-Naeini, J. Chan, F. Marquardt, O. Painter, Nonlinear radiation pressure dynamics in an optomechanical crystal. *Phys. Rev. Lett.* **115**, 233601 (2015).
43. D. Cattiaux, X. Zhou, S. Kumar, I. Golokolenov, R. R. Gazizulin, A. Luck, L. M. de Lépinay, M. Sillanpää, A. D. Armour, A. Fefferman, E. Collin, Beyond linear coupling in microwave optomechanics. *Phys. Rev. Res.* **2**, 033480 (2020).
44. H. Choi, M. Heuck, D. Englund, Self-similar nanocavity design with ultrasmall mode volume for single-photon nonlinearities. *Phys. Rev. Lett.* **118**, 223605 (2017).
45. E. Gil-Santos, C. Baker, D. T. Nguyen, W. Hease, C. Gomez, A. Lemaître, S. Ducci, G. Leo, I. Favero, High-frequency nano-optomechanical disk resonators in liquids. *Nat. Nanotechnol.* **10**, 810–816 (2015).
46. P. Kittel, Orbital resupply of liquid helium. *J. Spacecr. Rockets* **23**, 391–396 (1986).
47. S. Kurihara, Large-amplitude quasi-solitons in superfluid films. *J. Physical Soc. Japan* **50**, 3262–3267 (1981).
48. S. Kaminski, L. L. Martin, S. Maayani, T. Carmon, Ripplon laser through stimulated emission mediated by water waves. *Nat. Photonics* **10**, 758–761 (2016).
49. C. Ma, P. Yu, W. Wang, Y. Zhu, F. Lin, J. Wang, Z. Jing, X.-T. Kong, P. Li, A. O. Govorov, D. Liu, H. Xu, Z. Wang, Chiral optofluidics with a plasmonic metasurface using the photothermal effect. *ACS Nano* **15**, 16357–16367 (2021).
50. F. Luo, J. Yang, R. Zhou, Y. Li, T. Luan, Z. Li, J. Wu, Q. Shou, X. Xing, Highly efficient and controllable micromixer through interactions of photothermal multivortices. *Phys. Fluids* **34**, 072011 (2022).
51. R. Zhou, J. Yang, J. Yang, Y. Zhang, F. Luo, Y. Chen, Y. Li, T. Luan, Q. Shou, X. Jiang, X. Hu, J. Wu, C. Liu, H. Zhong, Z. Li, H.-P. Ho, X. Xing, Vortices-interaction-induced microstreaming for the pump-free separation of particles. *Optics Lett.* **46**, 3629–3632 (2021).
52. A. Ashkin, J. M. Dziedzic, Radiation pressure on a free liquid surface. *Phys. Rev. Lett.* **30**, 139–142 (1973).
53. C. Monat, P. Domachuk, B. J. Eggleton, Integrated optofluidics: A new river of light. *Nat. Photonics* **1**, 106–114 (2007).
54. R. Dahan, L. L. Martin, T. Carmon, Droplet optomechanics. *Optica* **3**, 175 (2016).
55. M. L. Douvidzon, S. Maayani, L. L. Martin, T. Carmon, Light and capillary waves propagation in water fibers. *Sci. Rep.* **7**, 16633 (2017).
56. S. Maayani, L. L. Martin, S. Kaminski, T. Carmon, Cavity optocapillaries. *Optica* **3**, 552 (2016).
57. I. S. Maksymov, A. D. Greentree, Coupling light and sound: Giant nonlinearities from oscillating bubbles and droplets. *Nanophotonics* **8**, 367–390 (2019).
58. J. Rosenberg, Q. Lin, O. Painter, Static and dynamic wavelength routing via the gradient optical force. *Nat. Photonics* **3**, 478–483 (2009).
59. C. Sun, M. Wade, M. Georgas, S. Lin, L. Alloatti, B. Moss, R. Kumar, A. H. Atabaki, F. Pavanello, J. M. Shainline, J. S. Orcutt, R. J. Ram, M. Popović, V. Stojanović, A 45 nm CMOS-SOI monolithic photonics platform with bit-statistics-based resonant microring thermal tuning. *IEEE J. Solid-State Circuits* **51**, 893–907 (2016).
60. X. He, C. Baker, Y. Sachkou, A. Sawadsky, S. Forstner, Y. Sfendla, and W. Bowen, Phonon Confinement by the Force of Light, in *CLEO Pacific Rim Conference*, (Hong Kong), p. Tu3F.3, OSA, (2018).
61. W. W. Wasserman, R. A. Harrison, G. I. Harris, A. Sawadsky, Y. L. Sfendla, W. P. Bowen, C. G. Baker, Cryogenic and hermetically sealed packaging of photonic chips for optomechanics. *Opt. Express* **30**, 30822–30831 (2022).
62. A. B. Matsko, V. S. Ilchenko, Optical resonators with whispering-gallery modes-part I: Basics. *IEEE J. Sel. Top. Quantum Electronics* **12**, 3–14 (2006).
63. D. R. Tilley, J. Tilley, Superfluidity and superconductivity, (CRC Press, 1990).
64. A. D. Kashkanova, A. B. Shkarin, C. D. Brown, N. E. Flowers-Jacobs, L. Childress, S. W. Hoch, L. Hohmann, K. Ott, J. Reichel, J. G. E. Harris, Superfluid Brillouin optomechanics. *Nat. Phys.* **13**, 74–79 (2017).
65. A. Shkarin, A. Kashkanova, C. Brown, S. Garcia, K. Ott, J. Reichel, J. Harris, Quantum optomechanics in a liquid. *Phys. Rev. Lett.* **122**, 153601 (2019).
66. G. I. Harris, A. Sawadsky, Y. L. Sfendla, W. W. Wasserman, W. P. Bowen, C. G. Baker, Proposal for a quantum traveling Brillouin resonator. *Opt. Express* **28**, 22450–22461 (2020).
67. F. Souris, X. Rojas, P. Kim, J. Davis, Ultralow-dissipation superfluid micromechanical resonator. *Phys. Rev. Appl.* **7**, 044008 (2017).
68. S. Schmid, L. G. Villanueva, M. L. Roukes, *Fundamentals of Nanomechanical Resonators*, (Cham: Springer International Publishing, 2016).

69. M. J. Moloney, Quality factors and conductances in helmholtz resonators. *Am. J. Phys.* **72**, 1035–1039 (2004).
70. H. Lamb, *Hydrodynamics*. 1916.
71. Y. L. Sfendla, C. G. Baker, G. I. Harris, L. Tian, R. A. Harrison, W. P. Bowen, Extreme quantum nonlinearity in superfluid thin-film surface waves. *npj Quantum Inf.* **7**, 1–12 (2021).
72. L. Ding, C. Baker, P. Senellart, A. Lemaitre, S. Ducci, G. Leo, I. Favero, High frequency GaAs nano-optomechanical disk resonator. *Phys. Rev. Lett.* **105**, 263903 (2010).
73. R. J. Donnelly, C. F. Barenghi, The observed properties of liquid helium at the saturated vapor pressure. *J. Phys. Chem. Ref. Data Monogr.* **27**, 1217–1274 (1998).
74. G. Sidebotham, *Heat Transfer Modeling*, (Cham: Springer International Publishing, 2015).
75. G. Swift, T. Molinski, W. Lehn, A fundamental approach to transformer thermal modeling. I. Theory and equivalent circuit. *IEEE Trans. Power Deliv.* **16**, 171–175 (2001).
76. J. Altet, A. Rubio, *Thermal Testing of Integrated Circuits*, (Boston, MA: Springer US, 2002).
77. K. J. Kontoleon, Dynamic thermal circuit modelling with distribution of internal solar radiation on varying façade orientations. *Energ. Buildings* **47**, 139–150 (2012).
78. Y. Gan, J. Wang, J. Liang, Z. Huang, M. Hu, Development of thermal equivalent circuit model of heat pipe-based thermal management system for a battery module with cylindrical cells. *Appl. Therm. Eng.* **164**, 114523 (2020).
79. M. P. Zaitlin, A. C. Anderson, Phonon thermal transport in noncrystalline materials. *Phys. Rev. B* **12**, 4475–4486 (1975).
80. R. C. Zeller, R. O. Pohl, Thermal conductivity and specific heat of noncrystalline solids. *Phys. Rev. B* **4**, 2029–2041 (1971).
81. G. L. Pollack, Kapitza resistance. *Rev. Mod. Phys.* **41**, 48–81 (1969).
82. E. Long, L. Meyer, Superfluidity and heat transport in the unsaturated helium-II film. *Phys. Rev.* **98**, 1616–1622 (1955).
83. H. Haus, *Waves and fields in optoelectronics*. Prentice-Hall, 1984.
84. D. Browne, Nonlinear effects in the damping of third-sound pulses. *J. Low Temp. Phys.* **57**, 207–226 (1984).
85. K. R. Atkins, C. E. Chase, The velocity of first sound in liquid helium. *Proc. Phys. Soc. Sec. A* **64**, 826–833 (1951).
86. COMSOL Multiphysics Material Library; https://www.comsol.com/material-library.
87. A. K. Raychaudhuri, Origin of the plateau in the low-temperature thermal conductivity of silica. *Phys. Rev. B* **39**, 1927–1931 (1989).
88. J. Rumble, *CRC handbook of chemistry and physics*. (CRC Press LLC, 2017).
89. R. A. Barton, I. R. Storch, V. P. Adiga, R. Sakakibara, B. R. Cipriany, B. Ilic, S. P. Wang, P. Ong, P. L. McEuen, J. M. Parpia, H. G. Craighead, Photothermal self-oscillation and laser cooling of graphene optomechanical systems. *Nano Lett.* **12**, 4681–4686 (2012).
90. R. De Alba, T. S. Abhilash, R. H. Rand, H. G. Craighead, J. M. Parpia, Low-Power Photothermal Self-Oscillation of Bimetallic Nanowires. *Nano Lett.* **17**, 3995–4002 (2017).
91. D. Woolf, P.-C. Hui, E. Iwase, M. Khan, A. W. Rodriguez, P. Deotare, I. Bulu, S. G. Johnson, F. Capasso, M. Loncar, Optomechanical and photothermal interactions in suspended photonic crystal membranes. *Opt. Express* **21**, 7258–7275 (2013).
92. P. E. Allain, B. Guha, C. Baker, D. Parrain, A. Lemaître, G. Leo, I. Favero, Electro-optomechanical modulation instability in a semiconductor resonator. *Phys. Rev. Lett.* **126**, 243901 (2021).
93. L. Mercadé, L. L. Martín, A. Griol, D. Navarro-Urrios, A. Martínez, Microwave oscillator and frequency comb in a silicon optomechanical cavity with a full phononic bandgap. *Nanophotonics* **9**, 3535–3544 (2020).
94. I. Ghorbel, F. Swiadek, R. Zhu, D. Dolfi, G. Lehoucq, A. Martin, G. Moille, L. Morvan, R. Braive, S. Combrié, A. De Rossi, Optomechanical gigahertz oscillator made of a two photon absorption free piezoelectric III/V semiconductor. *APL Photonics* **4**, 116103 (2019).
95. H. Jayakumar, B. Khanaliloo, D. P. Lake, P. E. Barclay, Tunable amplification and cooling of a diamond resonator with a microscope. *Phys. Rev. Appl.* **16**, 014063 (2021).
96. I. S. Grudinin, H. Lee, O. Painter, K. J. Vahala, Phonon laser action in a tunable two-level system. *Phys. Rev. Lett.* **104**, 083901 (2010).
97. W. C. Jiang, X. Lu, J. Zhang, Q. Lin, High-frequency silicon optomechanical oscillator with an ultralow threshold. *Opt. Express* **20**, 15991–15996 (2012).
98. Q. Lin, J. Rosenberg, X. Jiang, K. Vahala, O. Painter, Mechanical oscillation and cooling actuated by the optical gradient force. *Phys. Rev. Lett.* **103**, 103601 (2009).
99. F. M. Ellis, H. Luo, Third sound: Where are the solitons? *J. Low Temp. Phys.* **89**, 115–124 (1992).
100. F. Pobell, *Matter and methods at low temperatures*, (Springer, ed. 3, 2007).
101. W. B. Gauster, Low-temperature grüneisen parameters for silicon and aluminum. *Phys. Rev. B* **4**, 1288–1296 (1971).

Acknowledgments: We acknowledge the facilities and the scientific and technical assistance of the Microscopy Australia Facility at the Centre for Microscopy and Microanalysis (CMM), The University of Queensland. **Funding:** This work was funded by the U.S. Army Research Office through grant number W911NF17-1-0310 and the Australian Research Council Centre of Excellence for Engineered Quantum Systems (EQUS, project number CE170100009). C.G.B. and G.I.H., respectively, acknowledge Australian Research Council Fellowships DE190100318 and DE210100848. **Author contributions:** Data acquisition was performed by A.S. and C.G.B, with assistance from R.A.H., G.I.H., and W.W.W. A.S. fabricated the devices, and A.S., R.A.H., G.I.H., W.W.W., Y.L.S., and C.G.B. contributed to building the experimental setup. Theory development and data analysis were performed by A.S., R.A.H., G.I.H., W.P.B., and C.G.B. Numerical modeling was performed by A.S. with contributions from Y.L.S. Manuscript and figure preparation was performed by A.S., C.G.B., and W.P.B., with contributions from G.I.H. All authors provided feedback on the manuscript. C.G.B. and W.P.B. led the project, with support from G.I.H. **Competing interests:** The authors declare that they have no competing interests. **Data and materials availability:** All data needed to evaluate the conclusions in the paper are present in the paper and/or the Supplementary Materials. Additional simulation files and scripts are accessible from the Zenodo data repository https://doi.org/10.5281/zenodo.6982289.

Submitted 18 August 2022
Accepted 19 April 2023
Published 24 May 2023
10.1126/sciadv.ade3591

Science Advances

Engineered entropic forces allow ultrastrong dynamical backaction

Andreas Sawadsky, Raymond A. Harrison, Glen I. Harris, Walter W. Wasserman, Yasmine L. Sfendla, Warwick P. Bowen, and Christopher G. Baker

Sci. Adv., **9** (21), eade3591.
DOI: 10.1126/sciadv.ade3591

Science Advances (ISSN) is published by the American Association for the Advancement of Science. 1200 New York Avenue NW, Washington, DC 20005. The title *Science Advances* is a registered trademark of AAAS.